

Quantifying the single scattering albedo for the January 2017 Chile wildfires from simulations of the OMI absorbing aerosol index

Jiyunting Sun^{1,2}, J. Pepijn Veefkind^{1,2}, Peter van Velthoven¹, Pieter F. Levelt^{1,2}

¹Royal Netherlands Meteorological Institute, De Bilt, 3731 GA, the Netherlands

5 ²Department of Geoscience and Remote Sensing (GRS), Civil Engineering and Geosciences, Delft University of Technology, Delft, 2628 CD, the Netherlands

Correspondence to: Jiyunting Sun (jiyunting.sun@knmi.nl)

Abstract. The absorbing aerosol index (AAI) is a qualitative parameter directly calculated from satellite measured reflectance. Its sensitivity to absorbing aerosols in combination with a long-term data record since 1978 makes it an important parameter for climate research. In this study, we attempt to quantify aerosol absorption by retrieving the single scattering albedo (ω_0) at 550 nm from the satellite measured AAI. In the first part of this study, AAI sensitivity studies are presented exclusively for biomass burning aerosols. Later on, we employ a radiative transfer model (DISAMAR) to simulate the AAI measured by the Ozone Monitoring Instrument (OMI) in order to derive ω_0 at 550 nm. Inputs for the radiative transfer calculations include satellite measurement geometry and surface conditions from OMI, aerosol optical thickness (τ) from the MODerate-resolution Imaging Spectroradiometer (MODIS), and aerosol micro-physical parameters from the AERosol RObotic NETwork (AERONET), respectively. This approach is applied to the Chile wildfires for the period from 26 to 30 January 2017, when the OMI observed AAI of this event reached its peak. The Cloud and Aerosol Lidar with Orthogonal Polarization (CALIOP) overpasses missed the evolution of the smoke plume over the research region, therefore the aerosol profile is parameterized. The simulated plume is at an altitude of 4.5–4.9 km, which is in good agreement with available CALIOP backscatter coefficient measurements. Due to the data may contain pixels outside the plume, an outlier detection criterion is applied. The results show that the AAI simulated by DISAMAR is consistent with satellite observations. The correlation coefficients fall into the range between 0.85 and 0.95. The retrieved mean ω_0 at 550 nm for the entire plume over the research period from 26–30 January 2017 varies from 0.81 to 0.87, whereas the nearest AERONET station reported ω_0 is between 0.89 and 0.92. The difference in geolocation of the AERONET site and the plume, the assumption of homogeneous plume properties, the lack of the aerosol profile information, and the uncertainties in the inputs for radiative transfer calculation are primarily responsible for this discrepancy in ω_0 .

1 Introduction

Biomass burning aerosols are generated from combustion of carbon-containing fuels, either by natural or anthropogenic processes (Bond et al., 2004; IPCC, 2014). They are of great concern from the climate perspective (Kaufman and Boucher, 2002; IPCC, 2007; Koch and Del Genio, 2010; Huang et al., 2013; IPCC, 2014). The reported radiative forcing of black carbon (BC) produced by fossil fuel and biofuel is around 0.4 Wm^{-2} ($0.05 - 0.80 \text{ Wm}^{-2}$) (Ramanathan and Carmichael, 2008; Bond et al., 2013; Huang et al., 2013), but this estimate is highly uncertain. Accurate measurements of the aerosol single scattering albedo (ω_0) on a global scale can reduce the uncertainty in aerosol radiative forcing assessments (Hu et al., 2007). ω_0 is defined as the ratio of aerosol scattering over aerosol extinction. Currently ω_0 is mainly measured by ground-based instruments (Dubovik et al., 1998; Eck et al., 2003; Petters et al., 2003; Kassianov et al., 2005; Corr et al., 2009; Yin et al., 2015). Satellite sensors, such as the POLarization and Directionality of the Earth's Reflectances (POLDER), can retrieve ω_0 from a combination of multi-angular, multi-spectral observations of the polarized radiation. By measuring the anisotropy of the reflected radiance for each pixel, POLDER is expected to determine the reflected solar flux more accurately (Leroy et al., 1997). Unfortunately, there is no continuous record of ω_0 because the first two POLDER missions ended prematurely due to

40 technical problems, and the third POLDER mission only covered the period 2004-2014. Other satellite derived ω_0 is usually
 retrieved simultaneously with the aerosol optical thickness (τ) based on the pre-defined aerosol properties, such as the near-
 UV aerosol product (OMAERUV) of the Ozone Monitoring Instrument (OMI) on-board Aura (Torres et al., 2005; Torres et
 al., 2007). But this aerosol absorption over near-UV is highly sensitive to the assumption on aerosol layer height. Satheesh et
 al. (2009) therefore used the τ from MODerate-resolution Imaging Spectroradiometer (MODIS), which is independent of
 45 aerosol layer height, to constrain the OMAERUV retrieval. Their validation showed that compared with operational
 OMAERUV algorithm, the retrieved aerosol layer height by the hybrid method is in a better agreement with air-borne
 measurements, implying a potential improvement in aerosol absorption retrieval. This OMI-MODIS joint retrieval was also
 evaluated by Gassó and Torres (2016). They found that under less absorbing conditions, the hybrid method is sensitive to the
 variation in the input τ , which is used to select the retrieved pair of aerosol layer height and ω_0 .

50 Herman et al. (1997) first defined the near Ultra-Violet (UV) absorbing aerosol index (AAI), which provides an alternative
 methodology to retrieve ω_0 from satellite observations. The near-UV AAI, usually derived from the spectral range between
 340 and 390 nm, is a qualitative measure of absorbing aerosols that was first provided by the Total Ozone Mapping
 Spectrometer (TOMS) on-board Nimbus-7 in 1978. Since then several instruments have contributed to the AAI data record,
 which now spans over four decades. This long-term record is an important motivation for us to derive quantitative aerosol
 55 absorption information from the near-UV channel.

The most important advantage of the satellite retrieved AAI is that it does not depend on a-prior aerosol types, which are
 major uncertainties in aerosol parameter retrievals, such as τ . Ginoux et al. (2004) suggested that comparing model
 simulations with AAI from TOMS allows a better control of discrepancies because the only error source is from models.
 Further advantages of AAI are the low reflectivity of the Earth's surface and the absence of significant molecular absorption
 60 over the near-UV range. Using this band can ensure the aerosol absorption is one of the major contributors to the total signal.
 Moreover, the near-UV AAI is by definition highly sensitive to aerosol absorption. Previous studies have proven the
 potential of the near-UV AAI of TOMS in absorbing aerosol properties retrieval. Torres et al. (1998) provided the theoretical
 basis of an inversion method to derive τ and ω_0 from backscattered radiation. This method was validated by ground-based
 observations during the Southern African Regional Science Initiative (SAFARI) 2000 measurement campaign. The
 65 agreement of τ and ω_0 reaches $\pm 30\%$ and ± 0.03 , respectively (Torres et al., 2005). Hu et al. (2007) retrieved global
 columnar ω_0 based on the TOMS AAI with an average uncertainty of 15%.

This study is inspired by previous research to quantify the aerosol absorption from AAI. We use the near-UV AAI provided
 by OMI, the successor of TOMS, to derive the aerosol properties of the central Chile (Pichilemu 34.39°S, 72.00°W and
 Constitución 35.33°S, 72.42°W) wildfires in January 2017. The series of fires were triggered by a combination of long-term
 70 drought and high temperature, and were regarded as the worst wildfire season in the national history (The Guardian, 2017).
 The fires led to massive losses of the local forestry industry (pine and eucalyptus forests) (NASA.gov, 2017). The smoke
 plume was transported away from the source regions towards the tropical area of the Pacific Ocean by north-westward winds
 (Fig. 1). In this study, we quantitatively retrieve the ω_0 of this smoke by simulating the near-UV AAI of OMI with the
 radiative transfer model Determining Instrument Specifications and Analysing Methods for Atmospheric Retrieval
 75 (DISAMAR). The aerosol inputs of DISAMAR includes the τ retrieved from MODIS on-board the NASA EOS Aqua
 satellite, the information on aerosol micro-physical parameters provided by AERONET, and parameterized aerosol profiles.
 In the next section, we provide a brief introduction on the near-UV AAI and its sensitivity to various parameters. The
 methodology and datasets are described in section 3. In section 4, retrieved results and uncertainty analysis of Chile 2017
 wildfires are discussed, followed by main conclusions in section 5.

80 2 AAI sensitivity studies based on DISAMAR

In this section, we first introduce the near-UV AAI. In the sensitivity analysis, we show that the AAI depends not only on aerosol parameters, but also on the surface conditions and the observational geometry. The sensitivity analysis in this study is only designed for biomass burning aerosols.

2.1 Near-UV AAI definition

85 The concept of the near-UV AAI was first conceived to detect UV-absorbing aerosols from the spectral contrast provided by TOMS observations, known as the residue method (Herman et al., 1997). The basic idea of the residue method is that in a pure Rayleigh atmosphere, the reflectance (or equivalently the radiance (I_λ)) decreases strongly with the wavelength. The presence of absorbing aerosols will reduce this spectral dependency of I_λ . The change in this wavelength dependency is summarized as the AAI, which is calculated from the I_λ at the wavelength pair λ_1 and λ_2 ($\lambda_1 < \lambda_2$):

$$90 \text{ AAI} = -100 \left(\log_{10} \left(\frac{I_{\lambda_1}}{I_{\lambda_2}} \right)^{obs} - \log_{10} \left(\frac{I_{\lambda_1}}{I_{\lambda_2}} \right)^{Ray} \right), \quad (1)$$

The *obs* and *Ray* denote the I_λ is measured by satellite and calculated using a Rayleigh atmosphere, respectively. The longer wavelength λ_2 is treated as the reference wavelength where the surface albedo (a_s) is determined by fitting the observed radiance, i.e. $I_{\lambda_2}^{Ray}(a_s) = I_{\lambda_2}^{obs}$. This is done using an atmosphere containing only molecular scattering bounded by a Lambertian surface. The spectral dependency of a_s is neglected thus $I_{\lambda_1}^{Ray}$ is calculated using the same value as λ_2 . Defining

95 $\Delta I_{\lambda_1} = I_{\lambda_1}^{Ray} - I_{\lambda_1}^{obs}$, Eq.(1) can be rewritten as:

$$\text{AAI} = 100 \log_{10} \left(\frac{\Delta I_{\lambda_1}}{I_{\lambda_1}^{obs}} + 1 \right) \quad (2)$$

It is advantageous to use Eq.(2) because the AAI can be simply interpreted as the ratio between the simulated and observed radiance at λ_1 .

2.2 Near-UV AAI sensitivity studies

100 In this section, we present results of sensitivity studies performed by the radiative transfer model DISAMAR. DISAMAR can perform simulations of the forward I_λ spectrum in a wide spectral coverage (270 nm to 2.4 μm) and model scattering and absorption by gases, aerosols and clouds, as well as reflection by the surface (De Haan, 2011). It uses either the Doubling-Adding method or the Layer Based Orders of Scattering (LABOS) for the radiative transfer calculations. In this study the latter one is employed, because it is less computationally intensive (De Haan et al., 1987; De Haan, 2011).

105 DISAMAR allows to apply several aerosol scattering approximations. Here we assume Mie scattering aerosols. The parameters to describe Mie particles and their corresponding values are listed in Table 1. Considering the Chile wildfire plumes, which were dominated by biomass burning aerosols, these sensitivity studies are specifically performed for parameterized smoke aerosols, assuming only fine mode particles and weak linear wavelength dependency of the complex refractive index (n_r and n_i). The default values refer to observations of the daily average of the AERONET station

110 Santiago_Beauchef (33.46°S, 70.66°W) on January 27. We obtain the size distribution function and complex refractive index at 440, 675, 880 and 1018 nm from AERONET, and apply a linear interpolation / extrapolation to derive the complex refractive index over the spectrum from 340 to 675 nm, with spectral resolutions of 2 nm. Then DISAMAR uses above information to calculate the aerosol phase function $P(\Theta)$ and ω_0 over the full spectrum (340 to 675 nm). The corresponding $P(\Theta)$ at 354 nm for default case ($r_g = 0.15 \mu\text{m}$, $n_r = 1.5$ and $n_i = 0.06$) is presented in Fig.2. $P(\Theta)$ for other cases are provided

115 in the Appendix A (Fig.A1, A2 and A3). DISAMAR requires τ to be defined at 550 nm. Surface parameters include a spectrally flat a_s and the surface pressure P_s . The aerosol profile is parameterized as a single layer box shape, with its bottom

at $z_{aer}-\Delta z/2$ and top at $z_{aer}+\Delta z/2$, where z_{aer} and Δz are the geometric central height and the geometric thickness of the aerosol layer, respectively. The whole sensitivity analysis is performed for cloud-free condition. The wavelength pair of OMI (354 and 388 nm) is applied to compute the AAI. To make different sensitivity studies comparable, the AAI calculated in this section is normalized by the maximum value in each case. Note that sensitivity studies always use the default settings listed in Table 1 unless different values are explicitly mentioned.

Aerosol optical properties are determined by micro-physics, such as the real and imaginary part of the complex refractive index (n_r and n_i), and the particle size (r_g). Fig.3 shows how the variation of the AAI, $\Delta I_{\lambda 1}$, $I_{\lambda 1}^{obs}$ as well as of the optical properties (ω_0 and the asymmetry factor g) are associated with the complex refractive index and the particle size. The asymmetry factor g is the averaged cosine of the scattering angle Θ , weighted by $P(\Theta)$. Fig.3 shows that the effect of the complex refractive index is dual. As shown in Fig.3 (a), an increase in the real part of refractive index n_r directly enhances the magnitude of $I_{\lambda 1}^{obs}$, whereas $\Delta I_{\lambda 1}$ reduces. This results in low values of the AAI, which correspond to high ω_0 (Fig.3 (b)). Under the condition that measurement angle is $\Theta=150^\circ$, the declining g implies that more light is scattered in the line-of-sight of the detector, thus the higher $I_{\lambda 1}^{obs}$. Conversely, the imaginary part of refractive index n_i , which is directly associated with ω_0 , has an opposite influence, see Fig.3 (c) and (d). The particle size distribution has a more complicated influence on the AAI. As shown in Fig.3 (e), the AAI primarily follows the behaviour of $\Delta I_{\lambda 1}$, which decreases first and then increases when r_g is varying from 0.1 to 0.4 μm , whereas ω_0 is continuously decreasing and g is continuously increasing.

In addition to the micro-physics, the aerosol amount and distribution also have strong influences on the AAI. As shown in Fig.4 (a), the AAI is positively correlated with τ . The AAI is highly sensitive to the aerosol vertical distribution (Herman et al., 1997; Torres et al., 1998; de Graaf et al., 2005). As the aerosol layer ascends (Fig.4 (b)), more molecular scattering beneath the aerosol layer is shielded, which reduces $I_{\lambda 1}^{obs}$ while increases $\Delta I_{\lambda 1}$. The relation between the AAI and z_{aer} is almost linear. Fig.4 (c) shows that at the same altitude, the AAI slightly increases with the geometrical thickness of the aerosol layer. The reason could be that a larger Δz indicates the coming sunlight has a higher possibility to be absorbed by aerosols, slightly enhancing the aerosol absorption. Although the sensitivity exists, the impact is only up to 5%, which is negligible for practical purposes.

The calculated AAI does not only depend on aerosols themselves, but also on ambient conditions such as surface and clouds. Although the near-UV AAI is capable to distinguish absorbing and non-absorbing agents (Herman et al., 1997) and even to retrieve aerosol information over clouds (Torres et al., 2012), the uncertainty triggered by clouds is relatively high and therefore cloudy conditions are excluded from this study. Surface conditions are parameterized by P_s and a_s . It can be seen from Fig.5 (a) that a decrease in P_s , or equivalently an elevated terrain height, leads to less Rayleigh scattering shielded between the surface and the aerosol layer. As a result, the AAI decreases significantly due to smaller $\Delta I_{\lambda 1}$, in agreement with previous studies (de Graaf et al., 2005; Colarco et al., 2017). According to de Graaf et al. (2005), increasing a_s has two counteracting effects. On the one hand, it increases the amount of directly reflected radiation at the top of the atmosphere, namely a larger $I_{\lambda 1}^{obs}$, on the other hand it enhances the role of absorption by the aerosol layer rather than the surface, namely a larger $\Delta I_{\lambda 1}$. Which effect of a_s is dominant also depends on P_s (Fig.5 (b)). When the aerosol layer is relative to the sea level ($P_s = 1013$ hPa), the first effect dominates. However, a brighter surface compensates the loss of molecular scattering shielded by the aerosols when the terrain height rises ($P_s = 813$ hPa), which makes the absorbing layer more detectable.

The AAI also depends on the Sun-satellite geometry. Here we provide the AAI as a function of the measurement geometry for the default case with the relative azimuth angle $\Delta\phi = 180^\circ$. As presented in Fig.6 (a), the AAI becomes very sensitive to the geometries when zenith angles is larger than 60° , which confirms previous research (Herman et al., 1997; Torres et al., 1998; de Graaf et al., 2005). This is mainly due to the significant growth of $P(\Theta)$ when Θ becomes smaller (Fig.2). Thus, it is suggested that the OMI measurement with θ_0 larger than this value should be removed due to large variations in the AAI. To analyse the radiance behaviour as previously, we plotted the $I_{\lambda 1}^{obs}$ and $\Delta I_{\lambda 1}$ as a function of Θ along the cross section, respectively (Fig.6 (b)). It is noted that $I_{\lambda 1}^{obs}$ increases when Θ is larger than 90° , whereas the $P(\Theta)$ decreases at this range

160 (Fig.2). The reason could be that the Rayleigh scattering has an increasing contribution to the total radiance at those measurement angles (backscattering).

3 Methodology and datasets

In this section, we first present the datasets used and their pre-processing in this study, followed by the strategy to retrieve the aerosol ω_0 by constraining the simulated near-UV AAI with the observed one.

165 3.1 Datasets

3.1.1 OMI and GOME-2 absorbing aerosol index

The TOMS near-UV AAI retrieval has been proven a robust algorithm and applied to successive sensors, such as OMI on-board Aura and GOME-2 on-board MetOp-A/B. GOME-2 has higher spectral resolution (0.2-0.4 nm) than TOMS, but the spatial resolution is rather coarse (80×40 km²). In this study, GOME-2 measured AAI at wavelength pair 340 and 380 nm (http://archive.eumetsat.int) is only used as an independent dataset to assess the potential bias of the OMI measurements. OMI combines advantages of both TOMS and GOME-2. It covers wavelengths from 264 to 504 nm with a spectral resolution of approximately 0.5 nm and has a much higher spatial resolution than GOME-2 of 13×24 km² (Levelt et al., 2006). Note the GOME-2 and OMI have different equator crossing time (9:30 LT descending node for GOME-2 and 13:45 LT ascending node for OMI) that may affect the inter-comparison of the two satellite measurements.

175 Since the launch of OMI in 2004, the AAI retrieved from this instrument has been widely used in various applications. Kaskaoutis et al. (2010) employed the OMI measured AAI for regional research of the aerosol temporal and spatial distribution in Greece. Torres et al. (2012) utilized the advantage of near-UV AAI to detect aerosols over clouds. The OMI observed AAI was even used to evaluate the impact of surface dust loading on human health (Deroubaix et al., 2013). Buchar et al. (2015) also validated the NASA MERRA aerosol reanalysis product with the AAI retrieved from OMI.

180 In this study, the OMI level 2 product OMAERO (https://disc.gsfc.nasa.gov) is used to provide the AAI retrieved at the wavelength pair of 354 and 388 nm, and the corresponding viewing geometry and the surface condition when the measurements took place. The samples are included in the radiative transfer simulation only if θ_0 is smaller than 60°, and if satellite pixels are not contaminated by sun-glint, clouds, row anomalies or other errors of the instrument. The simulation is only applied to pixels inside the biomass burning plume, which is defined as AAI values larger than 1 for both OMI and

185 GOME-2.

3.1.2 MODIS and OMI aerosol optical thickness

MODIS on-board Aqua/Terra is a sensor that was specifically designed for atmosphere and climate research. The combination of two satellites ensures a daily global coverage. The spatial resolution ranges from 250 m to 1 km and it has 36 spectral bands from 400 nm to 14.4 μ m (Remer et al., 2005). MODIS employs separated algorithms for aerosol retrieval over oceans and land (Tanré et al., 1997; Kaufman and Tanré, 1998; Hsu et al., 2004; Remer et al., 2005). Currently the τ provided by MODIS is one of the most reliable datasets (Lee et al., 2009), with an estimated uncertainty of only 3-5% over ocean and 5-15% over land (Remer et al., 2005). Besides, the MODIS retrieved τ is free from the uncertainty triggered by assumed aerosol profile (Satheesh et al., 2009). As mentioned before, DISAMAR requires τ at 550 nm. This study uses cloud-filtered τ at 550 nm from the Collection 6 level 2 product MYD04 as the input for radiative transfer calculation

195 (https://ladsweb.modaps.eosdis.nasa.gov).

In addition, the τ measured by OMI and AERONET are compared with MODIS. The OMAERO τ retrieval uses multi-spectral fitting techniques. The retrieved τ is reported in good accordance with AERONET and is highly correlated with MODIS (Torres et al., 2007), with a correlation of 0.66 over land and 0.79 over oceans (Curier et al., 2008), although it

suffers from cloud contamination due to the relatively coarse spatial resolution of OMI. Considering the wavelength difference, the τ measured by OMI at 442 nm has to be transferred to 550 nm using the Ångström exponent (ÅE) 440 – 675 nm taken from AERONET near the time when OMI flies over the selected site. The AERONET dataset used in this study is introduced in the next section.

3.1.3 AERONET aerosol properties

AERONET is an aerosol monitoring network of ground-based sun photometers. With standardized instruments, calibration, processing and distribution, AERONET provides a long-term global database for aerosol research and air-borne and space-borne measurement validation. The system takes two basic measurements. The τ and ÅE are retrieved from the direct solar irradiance measurements; the r_g , $P(\Theta)$ (Nakajima et al., 1983; Nakajima et al., 1996), ω_0 (Dubovik et al., 1998), n_r and n_i (Dubovik and King, 2000) are derived from multiple-angular measurements of sky radiance.

The AERONET site nearest to the fire sources of 2017 Chile wildfires is the Santiago_Beauchef (33.46°S, 70.66°W) (<https://aeronet.gsfc.nasa.gov>). The dataset in use is version 2 level 1.5 product. To minimize the influence of temporal difference, the parameters of AERONET measured closest to the time of the OMI overpasses are used to simulate the optical properties of Mie scattering aerosols in DISAMAR. Note that the AERONET level 1.5 dataset is not quality-assured. In addition, the location of this AERONET site is in downtown of Santiago City and close to major roads, where the presence of scattering urban aerosols may bias the measurements of the plume.

The AERONET retrieved τ and ω_0 are used to evaluate the MODIS τ and retrieved ω_0 , respectively. The AERONET measured τ is transferred to 550 nm using the ÅE in range 440 – 675 nm while the ω_0 at 550 nm is linearly interpolated by values at 440 and 675 nm.

The AERONET inversion product needs to be processed into the inputs required by DISAMAR. Firstly, a conversion from the volume size distribution $V(r_v, \sigma_v)$ provided by AERONET to the number size distribution $N(r_g, \sigma_g)$ used in DISAMAR is required:

$$N(r_g, \sigma_g) = V(r_v, \sigma_v) \frac{3}{4\pi r_g^3} e^{-4.5\sigma_g^2}, \quad (4)$$

The following relation between the geometric and volumetric mean radii (r_g and r_v) and standard deviations (σ_g and σ_v) is assumed:

$$r_g = r_v e^{-3\sigma_g^2}, \quad (5)$$

$$\sigma_g = \sigma_v, \quad (6)$$

The fine and coarse mode particle size are derived by finding the two peaks of the log-normal distribution function provided by AERONET. The complex refractive index is assumed the same for both modes. Since bi-modal aerosol is not applicable in DISAMAR yet, we first calculate optical properties of two modes individually, then we externally combine the optical properties of two modes into a bi-modal aerosol with a fraction:

$$w_f = \frac{N_f(r_{g,f}, \sigma_{g,f})}{N_f(r_{g,f}, \sigma_{g,f}) + N_c(r_{g,c}, \sigma_{g,c})}, \quad (7)$$

$$w_c = 1 - w_f, \quad (8)$$

Then the weights for calculating the total ω_0 of the mixed aerosol are:

$$w_{\sigma,f} = \frac{w_f \sigma_f}{w_f \sigma_f + w_c \sigma_c}, \quad (9)$$

$$w_{\sigma,c} = 1 - w_{\sigma,f}, \quad (10)$$

235 Where the σ_f and σ_c are the extinction cross section of the fine and coarse aerosols. The expansion coefficients of the mixed aerosol is weighed by the ω_0 of the fine and coarse aerosols ($\omega_{0,f}$ and $\omega_{0,c}$), respectively:

$$w_{\omega_{0,f}} = \frac{w_f \sigma_f \omega_{0,f}}{w_f \sigma_f \omega_{0,f} + w_c \sigma_c \omega_{0,c}}, \quad (11)$$

$$w_{\omega_{0,c}} = 1 - w_{\omega_{0,f}}, \quad (12)$$

240 The AERONET instrument at this site only covers the visible and infrared band (440 nm to 1018 nm) for sky radiance measurements, i.e. no aerosol inversion products at UV band. Due to the absence of observations, assumptions have to be made on the spectral dependency of aerosol properties to obtain their values in the near-UV range. The properties of biomass burning aerosols depend on the type of fuel, the procedure producing the smoke, the age of the smoke, and also the atmospheric conditions (Reid et al., 2005). Using measurements to constrain the input aerosol refractive index may reduce the uncertainties due to a-priori knowledge. Our treatment on the complex refractive index is as following: (1) take the complex refractive index at visible band (440 to 675 nm) from AERONET measurements; (2) linearly extrapolate the complex refractive index to near-UV band. The real part n_r for radiative transfer calculation is obtained in this step. A slight wavelength dependency of n_r is found (Fig.9 (a)); (3) for the imaginary part n_i , we multiply it (for the entire wavelength from UV to visible) with a scaling factor as we set it as a free parameter. By varying the value of the scaling factor, both the magnitude and the wavelength dependency of n_i can change to meet the requirement of retrieval (Fig.9 (b)).

250 3.1.4 CALIOP backscattering coefficient

The CALIOP on-board CALIPSO, which was launched in 2006, provides high-resolution profiles of aerosols and clouds. It has three channels with one measuring the backscattering intensity at 1064 nm and the rest measuring orthogonally polarized components at 532 nm backscattering intensity (Winker and Omar, 2006). Due to the limited spatial coverage, CALIOP did not observe the Chile wildfires plume for all the cases where the OMI observations available. We only use the total attenuated backscatter at 532 nm from level 1B Version 4.10 Standard data to evaluate the parameterized aerosol profiles (<https://eosweb.larc.nasa.gov/project/calipso>).

3.2 Methodology

In this study, we employ the radiative transfer model DISAMAR to simulate the near-UV AAI from OMI and to derive the ω_0 for a specific case, i.e. the Chile wildfires in January 2017. We select the period from 26 to 30 January 2017 (28 January is excluded due to a lack of data) when the AAI value reached its peak during the wildfire period.

260 The forward simulation consists of two major steps. First, DISAMR calculates the Mie aerosol optical properties with aerosol micro-physical information taken from AERONET measurements (r_g , n_r and n_i). As mentioned in Section 3.1.3, we set the spectral-dependent imaginary refractive index n_i as a free parameter to vary ω_0 . Then, DISAMAR operates radiative transfer calculation with the input aerosol properties and environmental conditions of OMI.

265 It is noted that the observed aerosol vertical distribution is limited for the Chile wildfires. Previous research suggested the AAI cannot be quantitatively used without τ or z_{aer} information (Gassó and Torres, 2016). Instead, we implement the same parameterization on the aerosol profile as in the sensitivity studies. Since the AAI dependency on Δz is minor (Fig.4 (c)), and to reduce the computational cost, Δz is set a constant of 2 km based on the information from the CALIOP measurements of backscattering coefficient (β) at 532 nm (Fig.7). The z_{aer} , to which the AAI is highly sensitive, is treated as an unknown variable to be retrieved together with ω_0 .

Consequently, with various combinations of z_{aer} and ω_0 , a lookup table (LUT) of the calculated AAI is constructed by radiative transfer calculations. It should be noted that for all pixels in the plume we assume the same aerosol microphysical properties as well as the same aerosol layer height. Pixels outside the plume (even they have AAI values larger than 1) may

275 have significantly different properties and this will affect the results. As shown in Fig.8, the distribution of OMI measurements is sparse in space. These geographical outliers may cause the heterogeneous properties of the plume. Consequently, we apply a data quality control procedure before retrieving ω_0 . First, we manually remove the pixels that are geographically isolated from the main plume. Furthermore, we remove potential outliers based on statistical tool. We filter the dataset using an outlier detection criterion based on the interquartile range (IQR) of the AAI difference between DISAMAR simulations and OMI measurements. According to Tukey's fences (Tukey, 1977), an AAI difference falling outside range between $Q1-1.5 \text{ IQR}$ and $Q3+1.5 \text{ IQR}$ may be regarded as an outlier and removed, where $Q1$ and $Q3$ are the first and third quartiles of the AAI difference, and the IQR is the range between $Q1$ and $Q3$. Only the pixels passing the outlier detection criterion are used to calculate the cost function (Eq.(13)):

$$\text{RMSE} = \sqrt{\frac{\sum_i^n (AAI_{DSM,i}^{\text{qualified}} - AAI_{OMI,i})^2}{n}}, \quad (13)$$

285 Here AAI_i indicates the AAI for i th satellite pixel of the selected OMI data; subscripts DSM and OMI indicate the DISAMAR simulation and the OMI observation, respectively. The combination of z_{aer} and ω_0 that leads to the minimum AAI residue is used as retrieval results.

Finally, the simulated AAI is compared with OMI observations. We also employ the independent data from GOME-2 as a reference to identify the potential bias of OMI. Similarly, the τ retrieved from OMI and AERONET serve as a reference to that of MODIS. The estimated aerosol layer height and ω_0 at 550 nm are evaluated with independent observations from CALIOP and AERONET, respectively.

4 Results and discussion

By applying the methodology described in the previous section, we quantitatively retrieved the aerosol layer height and ω_0 at 550 nm of the Chile 2017 wildfires by AAI simulation. The OMI measurements of the plume are displayed in Fig.8 (a) – (d). The presented satellite pixels are with AAI values larger than 1, and are free of cloud contamination, sun-glint and row anomaly of the instrument. Fortunately, the remaining data is still able to capture the main plume features. It can be clearly seen that from 26 to 30 January, the plume produced by wildfires in the central Chile was transported by the south-easterly trade wind from the continent towards the lower latitude region of the Pacific Ocean. The plume travelled over a distance of 3000 km during the period.

295 The vertical movement of the plume is given by CALIOP backscattering coefficient measurements (β) at 532 nm (Fig.7). The CALIOP overpasses closest to the plume are marked by a black dashed line in Fig.7. It is noted that due to the spatial coverage and the measuring time difference, CALIOP are not able to represent the entire plume detected by OMI. The aerosol layer captured by CALIOP is distributed from 2 km to 6 km, with an average height at approximately 4-5 km. The ascent of the plume was driven by the heat generated by the fires and aerosol sunlight absorption, as well as the atmospheric vertical motions.

305 Fig.8 (e) – (h) show the AAI simulation selected by the data quality control mentioned in Section 3.2. The spatial distribution of the simulated AAI shows similar patterns as the OMI observations. Some data points that are geographically isolated from the plume though their AAI values are larger than 1, e.g. in case 26 and 30 January, may differ strongly from what are observed inside the plume. Including these outliers in the optimization could bias the retrieved aerosol properties. This can also be seen in Fig.8 (i) – (l), where the points passing the data quality control described in Section 3.2 are highlighted in red color. By removing the outliers, the average spatial correlation coefficient reaches 0.90.

Table 2 lists the statistics of the qualified AAI data, in terms of the median, relative difference and RMSE. The median of measured AAI ranges from 2 to 4 during the research period. Except for 26 January, the median of the simulated AAI in

other cases is in good agreement with the measurements, with relative differences within $\pm 6\%$. The RMSE is only acceptable reflects that part of the plume cannot be fit by the assumed homogeneous aerosol properties in the forward simulation. The majority of the simulated AAI for 26 January is negatively biased, which is reflected by the small slope without an intercept correction in Fig.8 (i). A systematic bias in the inputs might cause this result. In terms of ω_0 , both the AERONET measured and the AAI retrieved aerosol absorption become weaker with time (Table 2). Although the simulated and observed AAI are in good agreement, the difference in ω_0 is significant. The mean of the retrieved ω_0 at 550 nm for the whole period is 0.84, contrast to the AERONET measurements with a mean value of 0.90.

There are many sources contributing to this discrepancy in ω_0 . First of all, the nearest site Santiago_Beauchef is not exactly in the primary biomass burning regions as mentioned in section 3.1.3. The AERONET site is located in downtown, where reflective urban or industrial aerosols may have been mixed with the smoke and enhanced the ω_0 . This would also affect the spectral dependency of the complex refractive index used to constrain the radiative transfer calculation. According to Table 2, the retrieved n_i reveals that the difference between 354 and 388 nm is less than 5%. This small spectral dependency of n_i is mainly determined by AERONET measurements in the visible band (dashed lines in Fig.9 (b)), whereas the effect of the scaling factor is minor in this case. We thus find a much weaker wavelength dependency than the value in Jethva and Torres (2011) study, where a 20% difference between the two UV wavelengths was applied to OMAERUV algorithm to achieve the result that 70% of the retrieved ω_0 differ less than ± 0.03 from the ω_0 from the AERONET measurements. This 20% spectral dependency adopted in their work is associated with findings of Kirchstetter et al. (2004). According to them, the absorbing Ångström exponent (ÅÅE) of urban pollution is near unit and of biomass burning aerosols ranges is approximately 2 between 300 nm to 1 μm . In terms of n_i , a 20% increase at 354 nm with respect to the value at 388 nm is equivalent to an ÅÅE value between 2.5 and 3, depending on the aerosol models of OMAERUV (Jethva and Torres, 2011). Hoffer et al. (2004) also found similar results. They conducted in situ measurements on humic-like substances (HULIS) of Amazonia biomass burning aerosols and found that around 35% - 50% light absorption occurred at 300 nm, whereas only around 15% at 400 nm. Bergstrom et al. (2007) also confirmed this conclusion from several field programs (SAFARI 2000, ACE Asia, PRIDE, TARFOX, INTEx-A). From the sensitivity study of Jethva and Torres (2011), a stronger spectral dependency of n_i between 354 and 388 nm would allow simulations to reach the same AAI with n_i at a relatively low level. In our study, this means to retrieve a lower ω_0 at 550 nm. The presence of non-absorbing aerosols may enhance the measured n_i at visible band and the linear extension would weaken the spectral dependency particularly in the UV spectral range. Furthermore, the AERONET inversion product is not error-free. The uncertainty of size distribution retrieval is minor for biomass burning aerosols (Dubovik et al., 2000), but under optically thick circumstances, even when retrievals are quality-assured (i.e. level 2 data), the reported accuracy of complex refractive index is 0.04 for n_r and 30%-50% for n_i , respectively (Dubovik et al., 2002). It is also reported that AERONET tends to underestimate the absorption of biomass burning aerosols compared with in situ measurements (Dubovik et al., 2002; Reid et al., 2004). The uncertainty of ω_0 is 0.03 under high aerosol loading ($\tau_{440} > 0.5$) and 0.05-0.07 under low aerosol loading (Dubovik et al., 2002; Holben et al., 2006). Last but not least, the spatial representation of the in situ instrument also concerns. Santese et al. (2007) showed that the selected AERONET aerosol parameters can be representative of a $300 \times 300 \text{ km}^2$ southeast Italy area. For the Chile wildfires with the most remote pixel over 3000 km away from the continent, the measurements at AERONET cannot fully represent the plume detected by the satellite.

Apart from AERONET itself, information from other datasets could also bias the estimate of aerosol absorption. Among all the inputs, the parameterization of the one-layer box-shape aerosol profile could be the largest error source. Although the influence of Δz on the AAI is limited (Fig.4 (c)), the AAI calculation highly depends on z_{aer} (Fig.4 (b)). As shown in Table 2, the estimated plume altitude varies from 4.5 to 4.9 km. As the black solid line indicated in Fig.7, the retrieved z_{aer} can approximately capture the measured plume height. The z_{aer} on 26 January seems overestimated because of the temporal and spatial difference. Concretely, CALIOP sampled the plume near the sources and close to the surface, while the plume

observed by OMI had been already elevated and transported to the open ocean. The lack of information on the real plume height makes it challenging to determine whether the plume height is responsible for the systematic bias in Fig.8 (i). Except for 26 January, z_{aer} in other cases is in good agreement with what CALIOP observed. Although the retrieved aerosol layer heights are convincing to some extent, one should keep in mind that CALIOP and OMI observations are not exactly co-located. Besides, the parameterized aerosol profiles may fail to represent the spatial variation of the plume. Therefore, the uncertainty cannot be directly determined due to the lack of validation data.

Among the four days for which we retrieved ω_0 , the value for 27 January is significantly lower than others. For this day the agreement in terms of z_{aer} with CALIOP is reasonable. We therefore explore the effect of observational biases of the AAI and τ on the retrieved ω_0 . We investigate the potential bias of these two datasets by plotting the histogram of the AAI measurement difference between GOME-2 and OMI (Fig.10 (a)), against the τ measurement difference between MODIS and OMI (Fig.10 (b), both are converted into 550 nm). It is clear that on 27 January, the AAI from OMI seems to be overestimated compared to GOME-2. Although the difference in instrumental design and wavelength pair choice for AAI retrieval, measurement conditions, etc., could contribute to the AAI discrepancy between GOME-2 and OMI, exploring the difference between the two datasets is beyond the scope of this study. In aspect of input aerosol concentration, the τ from MODIS could be potentially underestimated. Fitting a higher AAI with a lower input τ leads to an overestimation in aerosol absorption. Here, we analytically quantify the impact of τ for this specific case by systematically enhancing the τ of MODIS with a constant variation ($\Delta\tau$) added to all pixels, with the AAI level and the aerosol layer height unchanged. Fig.10 (c) presents how the AAI RMSE and the estimated ω_0 respond to the enhanced τ . It can be clearly seen that an increase in overall τ level by 0.07 raises ω_0 to 0.84 and optimizes the AAI simulation to a RMSE less than 0.45. If we apply this τ adaption, the retrieved ω_0 of 27 January becomes more consistent with the other days.

Apart from the observational errors in AERONET, OMI and MODIS data, the assumption that the plume features are homogeneous could also result in the discrepancy between the AAI retrieved and the AERONET measured ω_0 . In reality, the plume altitude, the optical properties and even the chemical compositions could vary from pixel to pixel, while our simulations cannot consider those effects.

5 Conclusions

Biomass burning is a major source of absorbing aerosols making a significant contribution to climate warming. Quantitatively characterizing the absorption of biomass burning aerosols is therefore important to reduce the uncertainty in assessments of global aerosol radiative forcing. Facing the lack of long-term ω_0 record, this study explores an approach to retrieve ω_0 based on reflectivity in the near-UV channel measured by OMI. Although AAI is not a geophysical parameter and depends on many factors, its independency from pre-defined aerosol types, its high sensitivity to aerosol absorption as well as its long-term data record, makes it an attractive parameter to aerosol research.

We test the retrieval of ω_0 for the wildfires happening in central Chile in January 2017. After filtering the data from outliers, high spatial correlation coefficients (0.85 to 0.95) reach between the simulated and observed AAI. The retrieved aerosol layer heights indicate the plume was elevated to height of 4.5-4.9 km during the research period. These results are in agreement with CALIOP measurements. This plume average of the retrieved ω_0 at 550 nm is approximately 0.84, which is 0.06 lower than that of AERONET retrieval. The sources for discrepancy includes: the location of the AERONET site that may bias the measured ω_0 and complex refractive index; the simplified parameterization of the aerosol profile; the insufficient spatial representativeness of a single AERONET site; the observational errors in the input aerosol micro-physics, τ , as well as AAI; and the assumption of homogeneous plume properties. We quantitatively analyze the uncertainty of τ for a specific case (27 January) when the estimated aerosol layer height is in good agreement with the CALIOP measurements. An improvement in retrieved ω_0 can be seen by adapting the magnitude of aerosol concentration.

This study proves the potential of utilizing OMI measured AAI to quantitatively characterize aerosol absorption such as ω_0 . Currently, it is challenging to retrieve and validate results without reliable aerosol profile information. In the future, the availability of daily global aerosol layer height data, e.g. the L2 aerosol layer height product of TROPOspheric Monitoring Instrument on-board Sentinel-5 Precursor (TROPOMI) that is under development (Sanders and de Haan, 2016), are expected to provide a stronger constraint on the forward calculation and to reduce the uncertainty in the retrieved aerosol properties. It is also reliable to retrieve aerosol absorption for each individual pixel with constraint of the aerosol layer height information. The problem due to the poor spatial representativeness of in situ measurements can then be eased by comparing with the satellite pixels nearby the ground-based instruments. Perhaps, more sophisticated assumptions on spectral-dependent aerosol absorption (e.g. steeper gradient of n_i in UV than visible band) have to be made and evaluated by other observational aerosol properties in UV spectral range, e.g. AERONET measured τ in UV band, instead of only depending on measured refractive index in visible band.

Acknowledgements

This work was performed in the framework of the KNMI Multi-Annual Strategic Research (MSO). The authors thank to NASA's GES-DISC, LAADS DAAC and ASDC for free online access of OMI, MODIS and CALIOP data. The authors also thank to the Centre for Climate Resilience Research (CR)² at University of Chile (CONICYT/FONDAP/15110009) providing the data of the Santiago_Beauchef AERONET station.

References

- Bergstrom, R. W., Pilewskie, P., Russell, P. B., Redemann, J., Bond, T. C., Quinn, P. K. and Sierau, B.: Spectral absorption properties of atmospheric aerosols, *Atmos. Chem. Phys.*, 7(23), 5937–5943, doi:10.5194/acp-7-5937-2007, 2007.
- Bond, T. C., Streets, D. G., Yarber, K. F., Nelson, S. M., Woo, J. H. and Klimont, Z.: A technology-based global inventory of black and organic carbon emissions from combustion, *J. Geophys. Res. D Atmos.*, 109, D14203, doi:10.1029/2003JD003697, 2004.
- Bond, T. C., Doherty, S. J., Fahey, D. W., Forster, P. M., Berntsen, T., Deangelo, B. J., Flanner, M. G., Ghan, S., Karcher, B., Koch, D., Kinne, S., Kondo, Y., Quinn, P. K., Sarofim, M. C., Schultz, M. G., Schulz, M., Venkataraman, C., Zhang, H., Zhang, S., Bellouin, N., Guttikunda, S. K., Hopke, P. K., Jacobson, M. Z., Kaiser, J. W., Klimont, Z., Lohmann, U., Schwarz, J. P., Shindell, D., Storelvmo, T., Warren, S. G. and Zender, C. S.: Bounding the role of black carbon in the climate system: A scientific assessment, *J. Geophys. Res. Atmos.*, 118, 5380–5552, doi:10.1002/jgrd.50171, 2013.
- Buchard, V., Silva, A. M., Colarco, P. R., Darmenov, A., Randles, C. A., Govindaraju, R., Torres, O. and Goddard, N.: Using the OMI aerosol index and absorption aerosol optical depth to evaluate the NASA MERRA Aerosol Reanalysis, *Atmos. Chem. Phys.*, 15, 5743–5760, doi:10.5194/acp-15-5743-2015, 2015.
- Colarco, P. R., Gassó, S., Ahn, C., Buchard, V., Dasilva, A. M. and Torres, O.: Simulation of the Ozone Monitoring Instrument aerosol index using the NASA Goddard Earth Observing System aerosol reanalysis products, *Atmos. Meas. Tech.*, 10(11), 4121–4134, doi:10.5194/amt-10-4121-2017, 2017.
- Corr, C. A., Krotkov, N., Madronich, S., Slusser, J. R., Holben, B., Gao, W., Flynn, J., Lefer, B., Kreidenweis, S. M., Collins, F., Sciences, E., County, B., Division, A. C., Resource, N., Collins, F., Branch, B. S. and Sciences, A.: Retrieval of aerosol single scattering albedo at ultraviolet wavelengths at the T1 site during MILAGRO, *Atmos. Chem. Phys.*, 9, 5813–5827, 2009.
- Curier, R. L., Veefkind, J. P., Braak, R., Veihelmann, B., Torres, O. and de Leeuw, G.: Retrieval of aerosol optical properties from OMI radiances using a multiwavelength algorithm: Application to western Europe, *J. Geophys. Res. Atmos.*, 113, D17S90, doi:10.1029/2007JD008738, 2008.

- Deroubaix, A., Martiny, N., Chiapello, I. and Marticorena, B.: Remote Sensing of Environment Suitability of OMI aerosol index to reflect mineral dust surface conditions : Preliminary application for studying the link with meningitis epidemics in the Sahel, *Remote Sens. Environ.*, 133, 116–127, doi:10.1016/j.rse.2013.02.009, 2013.
- 440 de Graaf, M., Stammes, P., Torres, O. and Koelemeijer, R. B. A.: Absorbing Aerosol Index: Sensitivity analysis, application to GOME and comparison with TOMS, *J. Geophys. Res. D Atmos.*, 110, D01201, doi:10.1029/2004JD005178, 2005.
- de Haan, J. F.: DISAMAR Algorithm description and background information, De Bilt, 2011.
- de Haan, Johan F., Bosma, P.B and Hovenier, J. W.: The adding method for multiple scattering of polarized light, *Astron. Astrophys.*, 183, 371–391, 1987.
- 445 Dubovik, O., Holben, B., Eck, T. F., Smirnov, A., Kaufman, Y. J., King, M. D., Tanré, D., Slutsker, I., Sciences, G. E. and Directorate, E. S.: Variability of Absorption and Optical Properties of Key Aerosol Types Observed in Worldwide Locations, *J. Atmos. Sci.*, 59(3), 590–608, doi:10.1175/1520-0469(2002)059<0590:VOAAOP>2.0.CO;2, 2002.
- Dubovik, O., Holben, B. N., Kaufman, Y. J., Yamasoe, M., Smirnov, A., Tanré, D. and Slutsker, I.: Single-scattering albedo of smoke retrieved from the sky radiance and solar transmittance measured from ground, *J. Geophys. Res.*, 103, 31903–
- 450 31923, doi:10.1029/98JD02276, 1998.
- Dubovik, O. and King, M. D.: A flexible inversion algorithm for retrieval of aerosol optical properties from Sun and sky radiance measurements, *J. Geophys. Res.*, 105, 20637–20969, doi:10.1029/2000JD900282, 2000.
- Dubovik, O., Smirnov, A., Holben, B. N., King, M. D., Kaufman, Y. J., Eck, T. F. and Slutsker, I.: Accuracy assessments of aerosol optical properties retrieved from Aerosol Robotic Network (AERONET) Sun and sky radiance measurements, *J.*
- 455 *Geophys. Res.*, 105, 9791–9806, doi:10.1029/2000JD900040, 2000.
- Eck, T. F., Holben, B. N., Ward, D. E., Mukelabai, M. M., Dubovik, O., Smirnov, A., Schafer, J. S., Hsu, N. C., Piketh, S. J., Queface, A., Roux, J. Le, Swap, R. J. and Slutsker, I.: Variability of biomass burning aerosol optical characteristics in southern Africa during the SAFARI 2000 dry season campaign and a comparison of single scattering albedo estimates from radiometric measurements, *J. Geophys. Res.*, 108, 8477, doi:10.1029/2002JD002321, 2003.
- 460 Eck, T. F., Holben, B. N., Reid, J. S., Mukelabai, M. M., Piketh, S. J., Torres, O., Jethva, H. T., Hyer, E. J., Ward, D. E., Dubovik, O., Sinyuk, A., Schafer, J. S., Giles, D. M., Sorokin, M., Smirnov, A. and Slutsker, I.: A seasonal trend of single scattering albedo in southern African biomass-burning particles : Implications for satellite products and estimates of emissions for the world ' s largest biomass-burning source, *J. Geophys. Res.*, 118, 6414–6432, doi:10.1002/jgrd.50500, 2013.
- 465 Gassó, S. and Torres, O.: The role of cloud contamination, aerosol layer height and aerosol model in the assessment of the OMI near-UV retrievals over the ocean, *Atmos. Meas. Tech.*, 9(7), 3031–3052, doi:10.5194/amt-9-3031-2016, 2016.
- Ginoux, P., Prospero, J. M., Torres, O. and Chin, M.: Long-term simulation of global dust distribution with the GOCART model: Correlation with North Atlantic Oscillation, *Environ. Model. Softw.*, 19, 113–128, doi:10.1016/S1364-8152(03)00114-2, 2004.
- 470 Herman, J. R., Bhartia, P. K., Torres, O., Hsu, C., Seftor, C. and Celarier, E.: Global distribution of UV-absorbing aerosols from Nimbus 7/TOMS data, *J. Geophys. Res.*, 102, 16911–16992, doi:10.1029/96JD03680, 1997.
- Holben, B. N., Eck, T. F., Slutsker, I., Smirnov, A., Sinyuk, A., Schafer, J., Giles, D., Dubovik, O. and Lille, U. S. T. De: AERONET's Version 2.0 quality assurance criteria, *Int. Soc. Opt. Photonics*, 6408, 64080Q, 2006.
- Hsu, N. C., Tsay, S. C., King, M. D. and Herman, J. R.: Aerosol properties over bright-reflecting source regions, *IEEE*
- 475 *Trans. Geosci. Remote Sens.*, 42, 557–569, doi:10.1109/TGRS.2004.824067, 2004.
- Hu, R. M., Martin, R. V. and Fairlie, T. D.: Global retrieval of columnar aerosol single scattering albedo from space-based observations, *J. Geophys. Res. Atmos.*, 112, D02204, doi:10.1029/2005JD006832, 2007.
- Hoffer, A., Gelencsér, A., Guyon, P., Kiss, G., Schmid, O., Frank, G. P., Artaxo, P. and Andreae, M. O.: Optical properties of humic-like substances (HULIS) in biomass-burning aerosols, *Atmos. Chem. Phys.*, 6(11), 3563–3570, doi:10.5194/acp-6-

- 480 3563-2006, 2006.
- IPCC, 2007: Climate Change 2007: Synthesis Report. Contribution of Working Groups I, II and III to the Fourth Assessment Report of the Intergovernmental Panel on Climate Change [Core Writing Team, Pachauri, R.K and Reisinger, A. (eds.)]. IPCC, Geneva, Switzerland, 104 pp.
- IPCC, 2014: Climate Change 2014: Synthesis Report. Contribution of Working Groups I, II and III to the Fifth Assessment Report of the Intergovernmental Panel on Climate Change [Core Writing Team, R.K. Pachauri and L.A. Meyer (eds.)].
- 485 IPCC, Geneva, Switzerland, 151 pp.
- Jethva, H., Torres, O., Sciences, P. and Space, G.: Satellite-based evidence of wavelength-dependent aerosol absorption in biomass burning smoke inferred from Ozone Monitoring Instrument, , 10541–10551, doi:10.5194/acp-11-10541-2011, 2011.
- Kaskaoutis, D.G.; Nastos, P.T.; Kosmopoulos, P.G.; Kambezidis, H.D.; Kharol, S.K. and Badarinath, K. V. S.: The Aura –
- 490 OMI Aerosol Index distribution over Greece, *Atmos. Res. J.*, 98, 28–39, doi:10.1016/j.atmosres.2010.03.018, 2010.
- Kassianov, E. I., Barnard, J. C. and Ackerman, T. P.: Retrieval of aerosol microphysical properties using surface MultiFilter Rotating Shadowband Radiometer (MFRSR) data : Modeling and observations, *J. Geophys. Res.*, 110, D09201, doi:10.1029/2004JD005337, 2005.
- Kaufman, Y. J., Tanré, D. and Boucher, O.: A Satellite View of Aerosols in the Climate System, *Nature*, 419, 215–223,
- 495 2002.
- Kirchstetter, T. W., Novakov, T. and Hobbs, P. V.: Evidence that the spectral dependency of light absorption by aerosols is affected by organic carbon, *J. Geophys. Res. D Atmos.*, 109(21), 1–12, doi:10.1029/2004JD004999, 2004.
- Koch, D. and Del Genio, A. D.: Black carbon semi-direct effects on cloud cover: Review and synthesis, *Atmos. Chem. Phys.*, 10, 7685–7696, doi:10.5194/acp-10-7685-2010, 2010.
- 500 Lee, K. H., Li, Z., Kim, Y. J. and Kokhanovsky, A.: Atmospheric Aerosol Monitoring from Satellite Observations: A History of Three Decades, in *Atmospheric and Biological Environmental Monitoring*, pp. 13–38., 2009.
- Leroy, M., Deuzé, J. L., Bréon, F. M., Hautecoeur, O., Herman, M., Buriez, J. C., Tanré, D., Bouffières, S., Chazette, P. and Roujean, J. L.: Retrieval of atmospheric properties and surface bidirectional reflectances over land from POLDER/ADEOS, *J. Geophys. Res.*, 102, 17023-17037, doi:10.1029/96JD02662, 1997.
- 505 Levelt, P. F., Oord, G. H. J. Van Den, Dobber, M. R., Mälkki, A., Visser, H., Vries, J. De, Stammes, P., Lundell, J. O. V and Saari, H.: The Ozone Monitoring Instrument, *IEEE Trans. Geosci. Remote Sens.*, 44, 1093–1101, 2006.
- Myhre, G., Shindell, D., Bréon, F. M., Collins, W., Fuglestad, J., Huang, J., ... & Nakajima, T.: Anthropogenic and Natural Radiative Forcing, *Clim. Chang.*, 432, 658–740, 2013.
- Nakajima, T., Tanaka, M. and Yamauchi, T.: Retrieval of the optical properties of aerosols from aureole and extinction data,
- 510 *Appl. Opt.*, 22, 2951–2959, 1983.
- Nakajima, T., Tonna, G., Rao, R., Boi, P., Kaufman, Y. and Holben, B.: Use of sky brightness measurements from ground for remote sensing of particulate polydispersions, *Appl. Opt.*, 35, 2672–2686, doi:10.1364/AO.35.002672, 1996.
- NASA.gov: NASA's Terra Catches Fires in Central Chile, [online] Available from: <https://www.nasa.gov/image-feature/goddard/2017/nasas-terra-catches-fires-in-central-chile> (Accessed 1 May 2017), 2017.
- 515 Petters, J. L., Saxena, V. K., Slusser, J. R., Wenny, B. N. and Madronich, S.: Aerosol single scattering albedo retrieved from measurements of surface UV irradiance and a radiative transfer model, *J. Geophys. Res.*, 108, 4288, doi:10.1029/2002JD002360, 2003.
- Ramanathan, V. and Carmichael, G.: Global and regional climate changes due to black carbon, *Nat. Geosci.*, 1, 221–227, doi:10.1038/ngeo156, 2008.
- 520 Reid, J. S., Eck, T. F., Christopher, S. A., Koppmann, R., Dubovik, O., Eleuterio, D. P., Holben, B. N., Reid, E. A. and Zhang, J.: A review of biomass burning emissions part III: intensive optical properties of biomass burning particles, *Atmos. Chem. Phys. Discuss.*, doi:10.5194/acpd-4-5201-2004, 2004.

- Remer, L.A., Kaufman, Y.J., Tanré, D., Mattoo, S., Chu, D.A., Martins, J.V., Li, R.R., Ichiku, C., Levy, R.C., Kleidman, R.G., Eck, T.K., Vermote, E. and Holben, B. N.: The MODIS Aerosol Algorithm, Products, and Validation, *J. Atmos. Sci.*, 62, 947–973, 2005.
- Remer, L.A., Tanré, D. and Kaufman, Y. J.: Algorithm for remote sensing of tropospheric aerosol from MODIS:Collection 5 Product ID: MOD04/MYD04-C005., 1998.
- Sanders, A.F.J. and de Haan, J.F: TROPOMI ATBD of the Aerosol Layer Height product, 2016.
- Stein Zweers, D.C: TROPOMI ATBD of the UV aerosol index., 2016.
- Santese, M., De Tomasi, F. and Perrone, M. R.: AERONET versus MODIS aerosol parameters at different spatial resolutions over southeast Italy, *J. Geophys. Res. Atmos.*, 112(10), 1–12, doi:10.1029/2006JD007742, 2007.
- Satheesh, S. K., Torres, O., Remer, L. A., Babu, S. S., Vinoj, V., Eck, T. F., Kleidman, R. G. and Holben, B. N.: Improved assessment of aerosol absorption using OMI-MODIS joint retrieval, *J. Geophys. Res. Atmos.*, 114(5), 1–10, doi:10.1029/2008JD011024, 2009.
- Tanr, D., J Kaufman, B. Y., Herman, M. and Mattoo, S.: Remote sensing of aerosol properties over oceans using the MODIS/EOS spectral radiances, *J. Geophys. Res.*, 102, 16971–16988, doi:10.1029/96JD03437, 1997.
- The Guardian: Chile battles devastating wildfires: 'We have never seen anything on this scale', [online] Available from: https://www.theguardian.com/world/2017/jan/25/chile-fire-firefighting-international-help?utm_source=Climate+News+Network&utm_campaign=afdf3cf10c-EMAIL_CAMPAIGN_2017_02_03&utm_medium=email&utm_term=0_1198ea8936-afdf3cf10c-38798061 (Accessed 25 Jan 2017), 2017.
- Torres, O., Bhartia, P. K., Herman, J. R., Ahmad, Z. and Gleason, J.: Derivation of aerosol properties from satellite measurements of backscattered ultraviolet radiation: Theoretical basis, *J. Geophys. Res. Atmos.*, 103, 17099–17110, doi:10.1029/98JD00900, 1998.
- Torres, O., Bhartia, P. K., Sinyuk, A., Welton, E. J. and Holben, B.: Total Ozone Mapping Spectrometer measurements of aerosol absorption from space: Comparison to SAFARI 2000 ground-based observations, *J. Geophys. Res. D Atmos.*, 110, D10S18, doi:10.1029/2004JD004611, 2005.
- Torres, O., Tanskanen, A., Veihelmann, B., Ahn, C., Braak, R., Bhartia, P. K., Veefkind, P. and Levelt, P.: Aerosols and surface UV products from Ozone Monitoring Instrument observations : An overview, *J. Geophys. Res.*, 112, D24S47, doi:10.1029/2007JD008809, 2007.
- Torres, O., Jethva, H. and Bhartia, P. K.: Retrieval of Aerosol Optical Depth above Clouds from OMI Observations: Sensitivity Analysis and Case Studies, *J. Atmos. Sci.*, 69, 1037–1053, doi:10.1175/JAS-D-11-0130.1, 2012.
- Tukey, J.W.: Exploratory data analysis, Addison-Wesley Publishing Company, 1977.
- Winker, D. M., Vaughan, M. A., Omar, A., Hu, Y., Powell, K. A., Liu, Z.;Hunt, W.H.;Young, S. A.: Overview of the CALIPSO Mission and CALIOP Data Processing Algorithms, *Technol. J. Atmos. Ocean.*, 26, 2310–2323, doi:10.1175/2009JTECHA1281.1, 2009.
- Yin, B., Min, Q. and Joseph, E.: Retrievals and uncertainty analysis of aerosol single scattering albedo from MFRSR measurements, *J. Quant. Spectrosc. Radiat. Transf.*, 150, 95–106, doi:10.1016/j.jqsrt.2014.08.012, 2015.

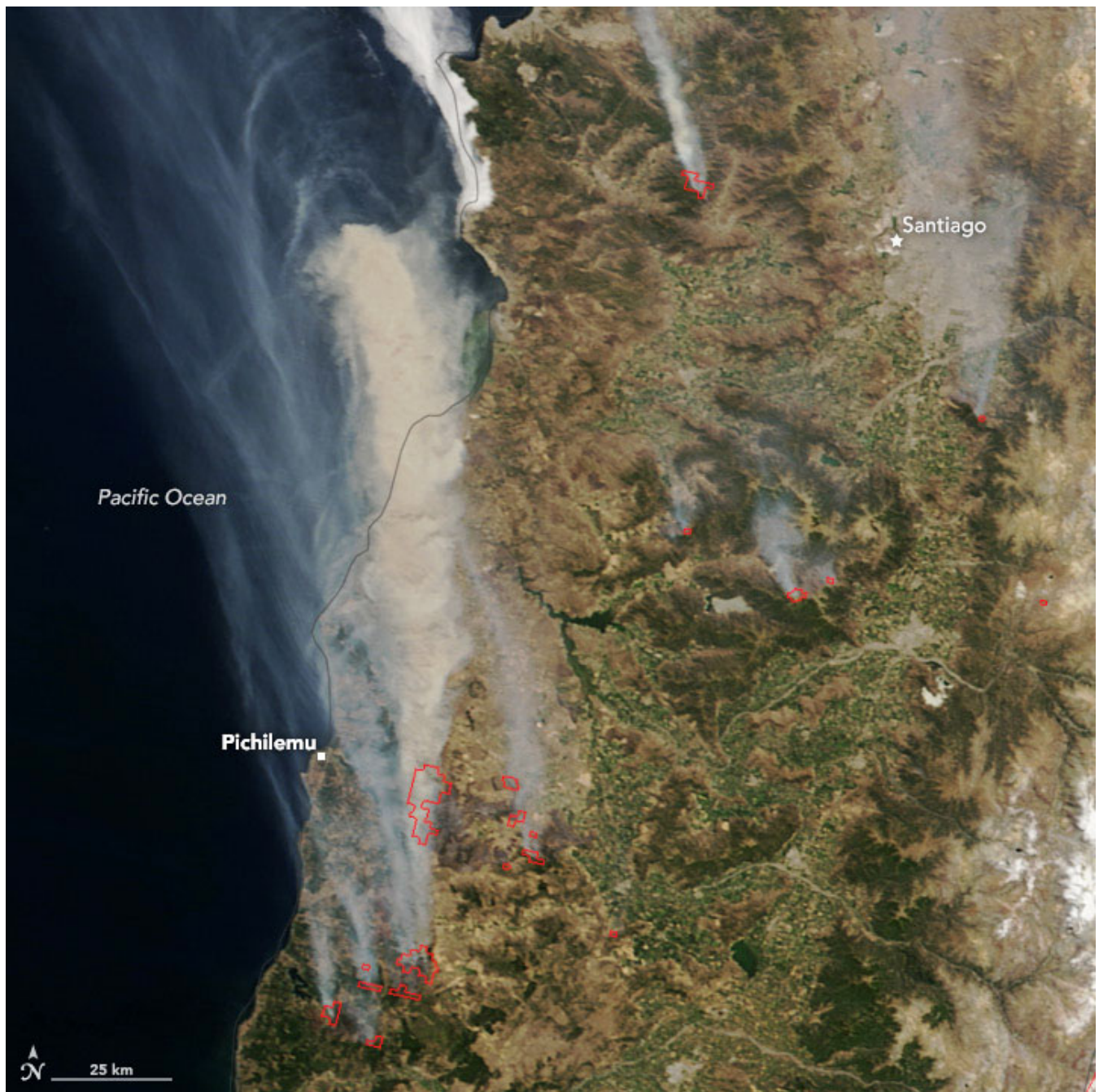


Figure 1: Chile wildfires detected by Terra/MODIS on 20 January 2017 (Image source: NASA's Earth Observatory <https://earthobservatory.nasa.gov/images/89496>).

565

570

575

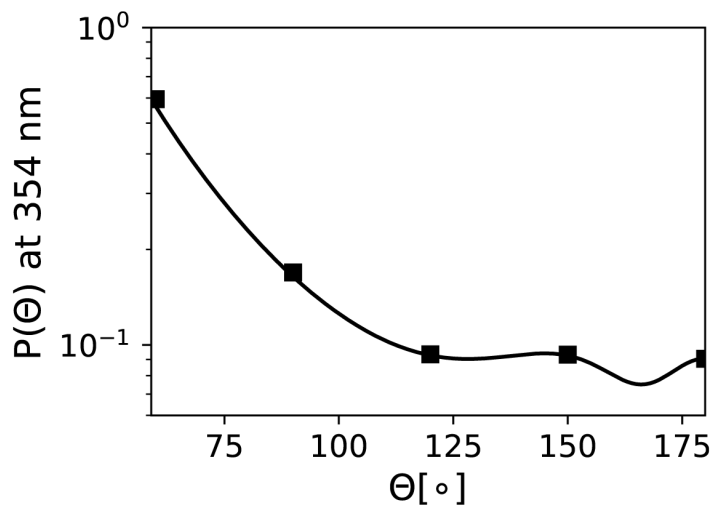


Figure 2: Phase function $p(\Theta)$ at 354 nm of the parameterized Mie scattering aerosol of default case ($r_g = 0.15 \mu\text{m}$, $n_r = 1.5$ and $n_i = 0.06$) in sensitivity analysis. The markers in the plot correspond to the value when $\Theta = 60^\circ, 90^\circ, 120^\circ, 150^\circ, 180^\circ$.

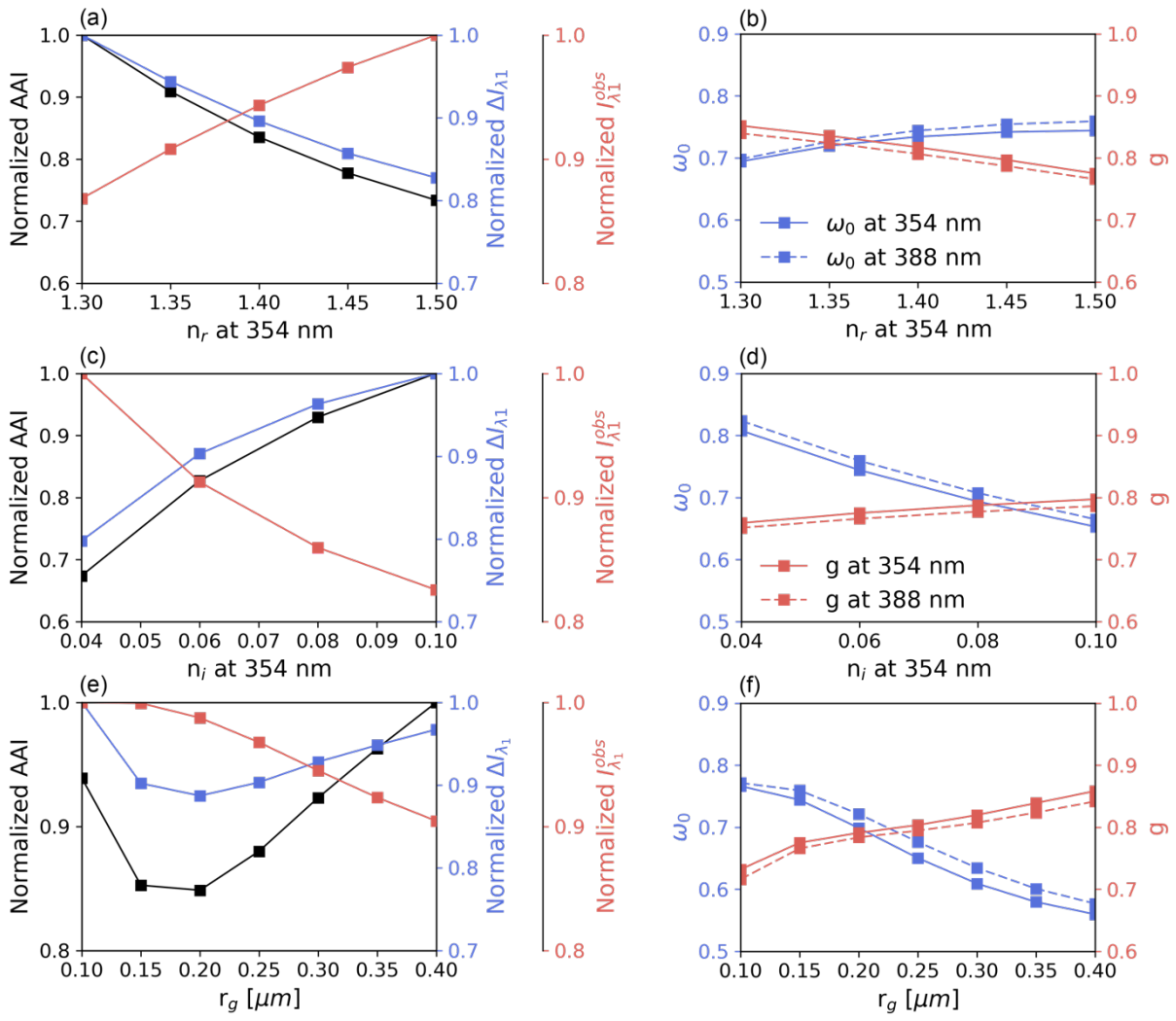


Figure 3: AAI sensitivity to micro-physical parameters: n_i (a, b), n_r (c, d), and r_g (e, f). The left panels (a, c and e) show the sensitivity of the normalized AAI (black), the normalized $\Delta I_{\lambda 1}$ (blue) and the normalized $I_{\lambda 1}^{obs}$ (red). The right panels (b, d and f) show ω_0 (blue) and g (red) at wavelength 354 (solid line) and 388 (dashed line) nm, respectively.

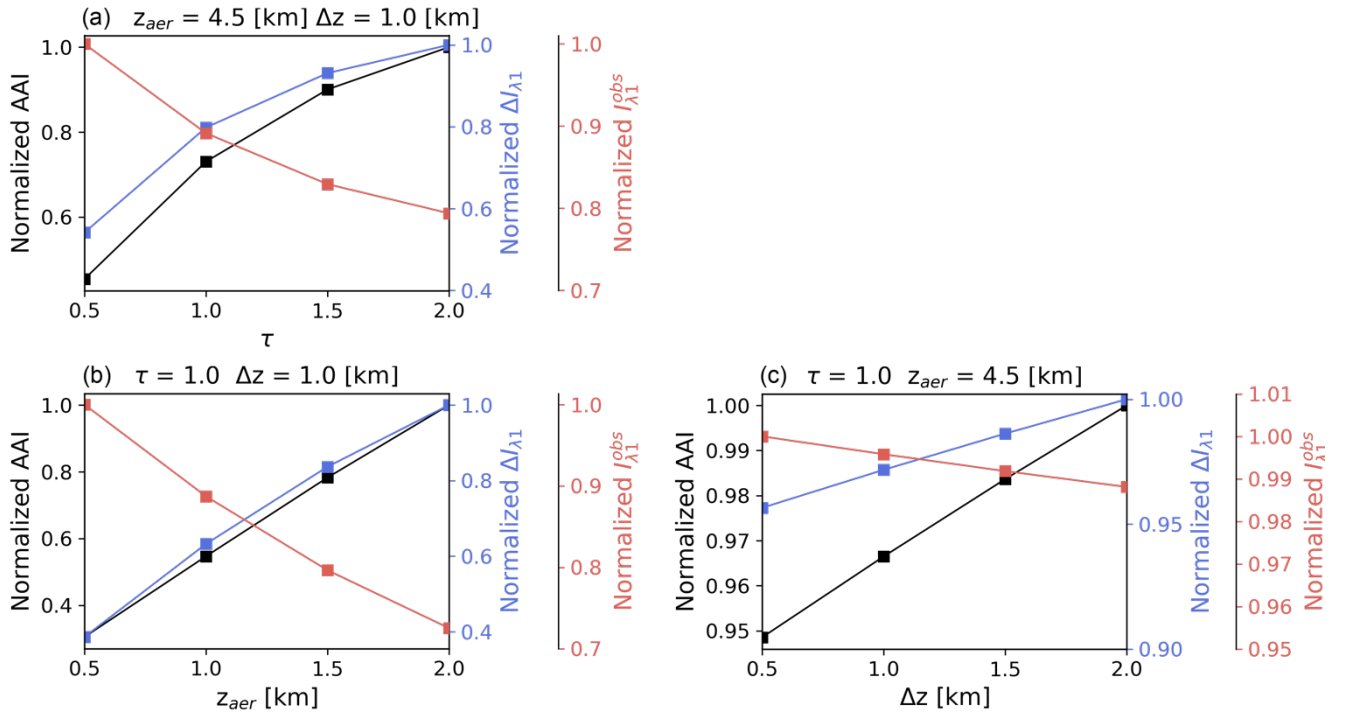


Figure 4: AAI sensitivity to macro-physical parameters: (a) τ at 550 nm, (b) z_{aer} and (c) Δz .

610

615

620

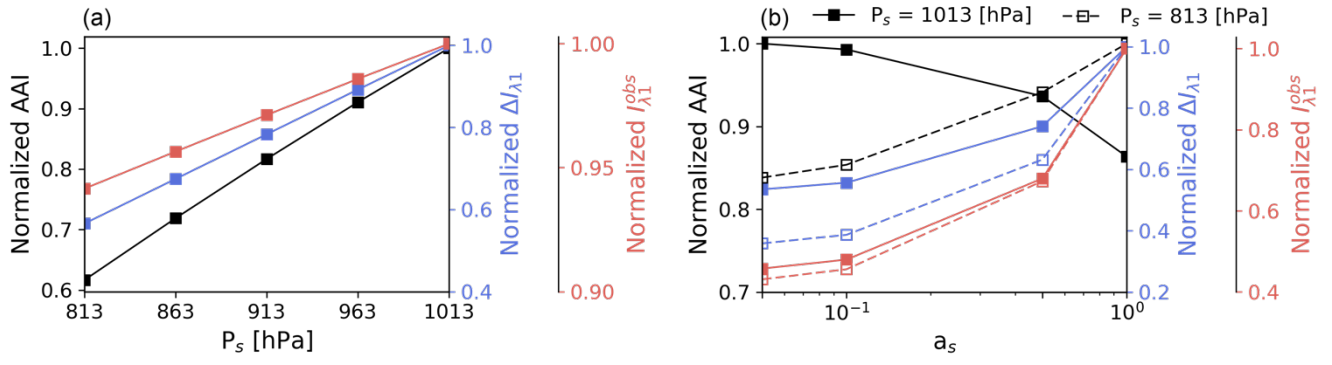


Figure.5 AAI sensitivity to surface parameters: P_s (a) and a_s (b). The solid line and dashed line in (b) indicate terrain height at sea level ($P_s = 1013$ hPa) and elevated terrain height ($P_s = 813$ hPa), respectively.

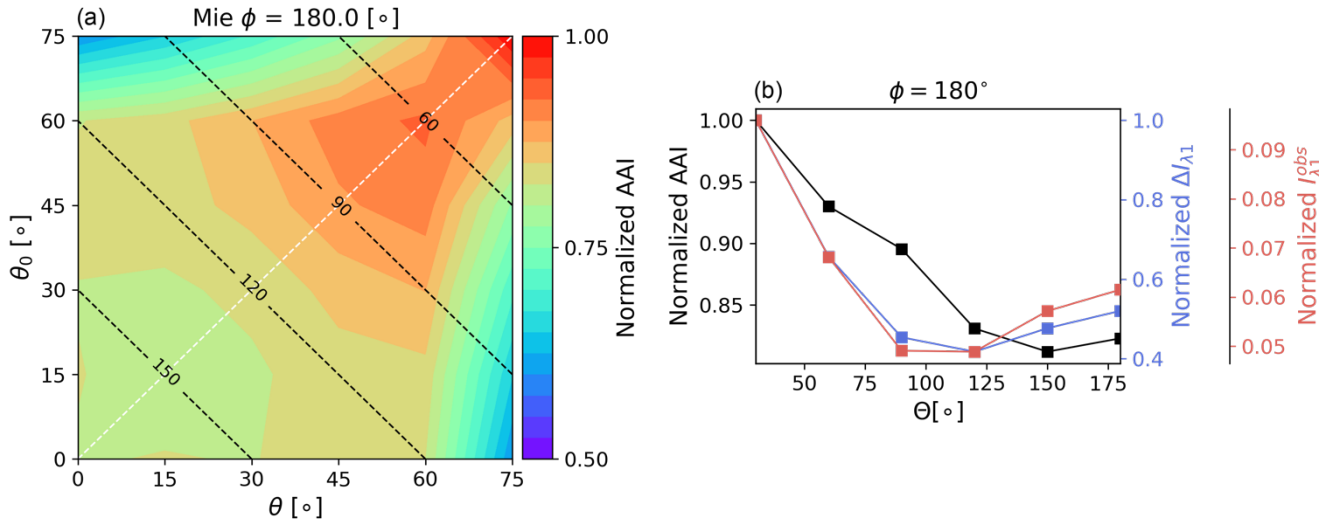
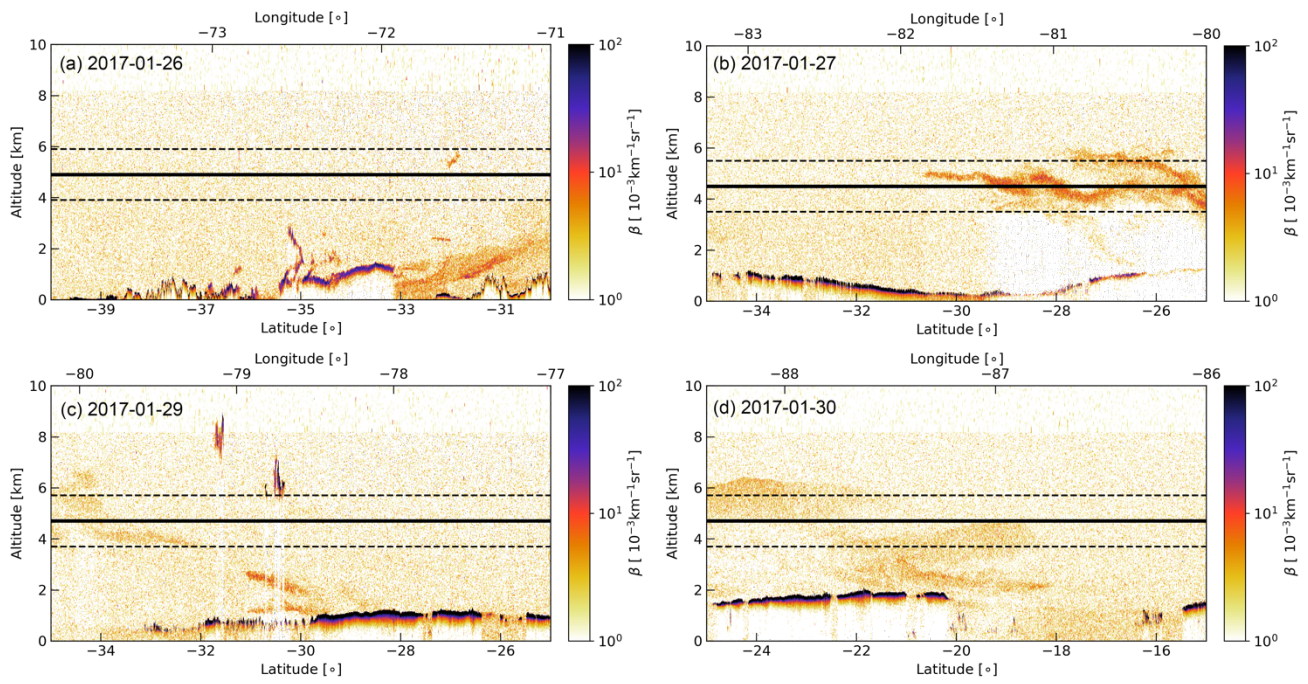


Figure.6 AAI sensitivity to θ and θ_0 at $\phi=180^\circ$. The black dashed contour in (a) indicates the $\Theta=60^\circ, 90^\circ, 120^\circ, 150^\circ$. The white dashed line in (a) indicates the cross section along viewing angles, with its corresponding normalized AAI, $\Delta I_{\lambda 1}$ and $I_{\lambda 1}^{obs}$ presented in (b).



675 **Figure.7 CALIOP backscatter coefficient β at 532 nm. The solid and dashed line indicate the retrieved z_{aer} and Δz , respectively. The red to black dots indicate clouds and the orange dots indicate aerosol layers, respectively.**

680

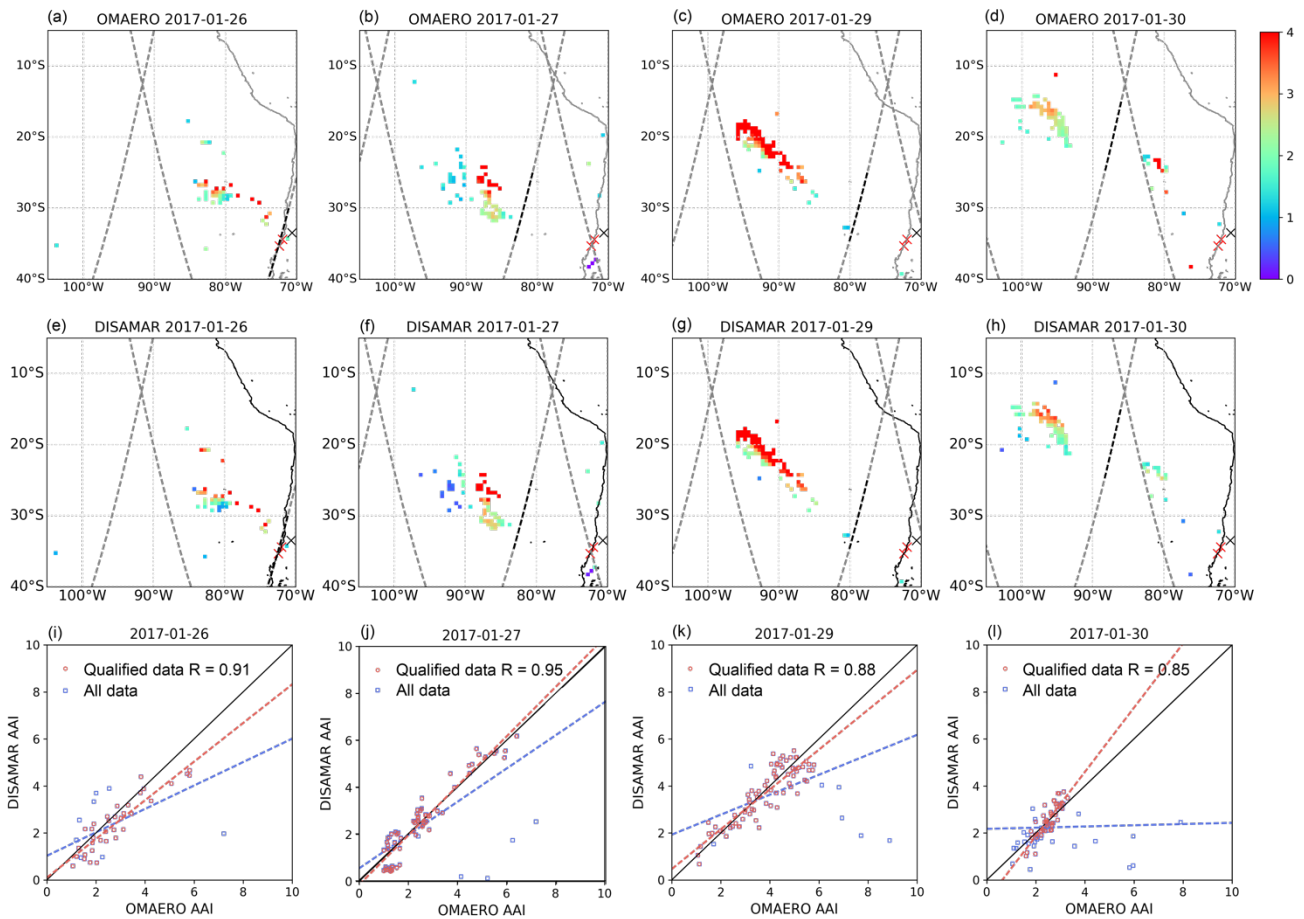


Figure.8 AAI from OMI observations (a–d) and DISAMAR simulations (e–h) of the Chile wildfires on 26, 27, 29 and 30 January 2017. The black and red cross symbols are the AERONET station and the main fire sources (Pichilemu W34.39° S72.00° and Consitución S35.33°, W72.42°), respectively. The grey dashed line indicates the CALIOP overpasses in the region of interest, where the overpasses used to validate the plume height are marked by black dashed line. The scatter plots (i–l) present the OMI observations against DISAMAR simulations for only qualified data (red dot) and all data (blue dot), respectively.

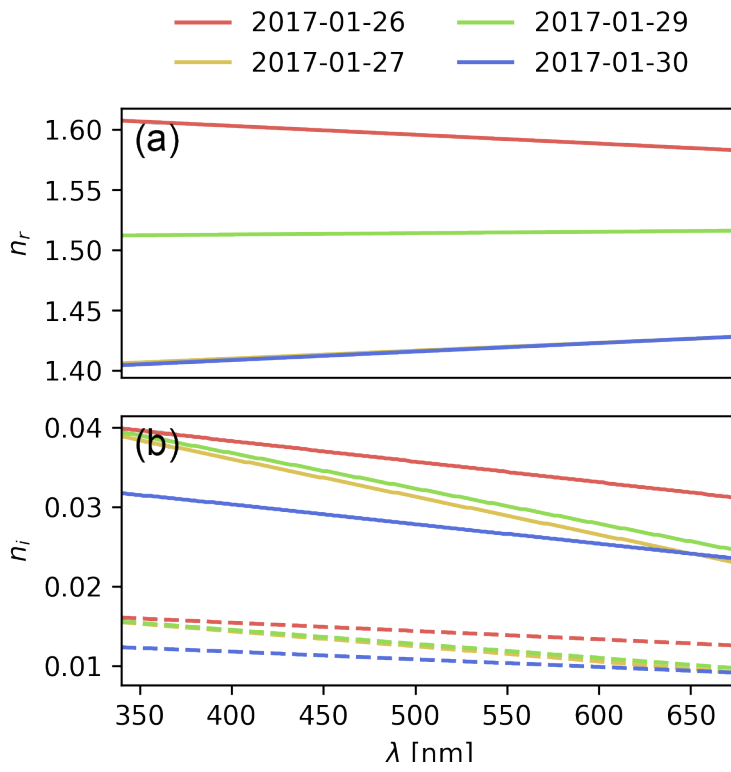


Figure.9 Retrieved complex refractive index for each case: (a) n_r and (b) n_i . The dashed line in lower panel is the wavelength dependent n_i measured by AERONET.

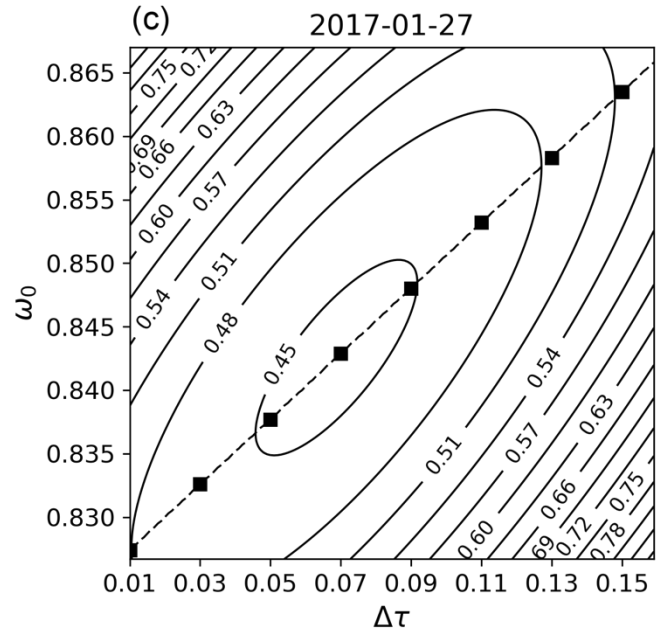
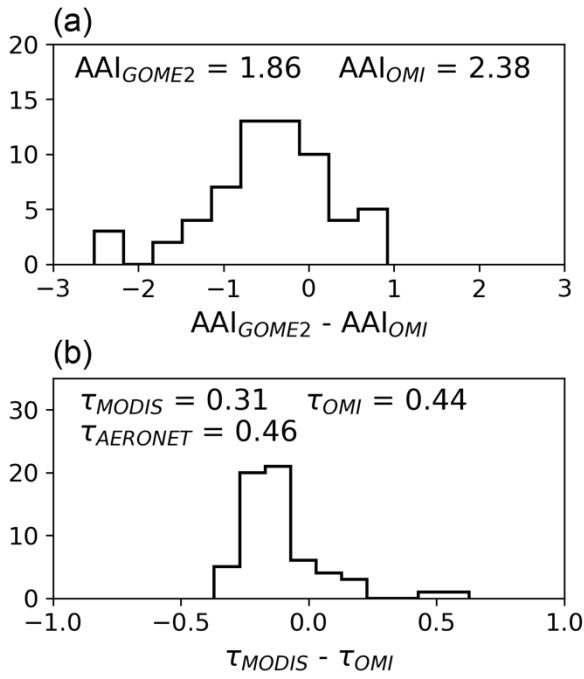


Figure.10 Histogram of (a) the AAI difference between GOME-2 and OMI, against (b) the τ difference at 550 nm between MODIS and OMI for 27 January. Contour of (c) the AAI RMSE as a function of variation in τ and ω_0 for 27 January. The dashed line is the best estimation for each pair of $\Delta\tau$ and ω_0 .

Table 1. Parameters used in sensitivity studies.

Parameters	Default value	Sensitivity range	Unit
Geometric mean radius (r_g)	0.15	0.1, 0.15, 0.2, 0.25, 0.3, 0.35, 0.4	μm
Geometric standard deviation (σ_g)	1.5	-	μm
Real refractive index (n_r) at 354 nm	1.5	1.3, 1.35, 1.4, 1.45, 1.5	-
Imaginary refractive index (n_i) at 354 nm	0.06	0.04, 0.06, 0.08, 0.1	-
Aerosol layer geometric central height (z_{aer})	4.5	2.5, 4.5, 6.5, 8.5	km
Aerosol layer geometric thickness (Δz)	1	0.5, 1, 1.5, 2	km
Aerosol optical thickness (τ) at 550 nm	1	0.5, 1, 1.5, 2	-
Surface albedo (a_s)	0.05	0.05, 0.1, 0.5, 1.0	-
Surface pressure (P_s)	1013	1013, 963, 913, 863, 813	hPa
Solar zenith angle (θ_0)	30	0, 15, 30, 45, 60, 75	$^\circ$
Viewing zenith angle (θ)	0	0, 15, 30, 45, 60, 75	$^\circ$
Relative azimuth angle ($\Delta\varphi = \varphi - \varphi_0 + 180^\circ$)	0	0, ± 45 , ± 90 , ± 135 , ± 180	$^\circ$

750

755

760

765

770

775

Table.2 Summary of retrieved results (after applying IQR outlier detection).

Date		2017-01-26	2017-01-27	2017-01-29	2017-01-30
Number of pixels in the plume		44	70	82	75
AAI	AAI median (OMAERO)	2.52	2.38	4.05	2.61
	AAI median (DISAMAR)	2.17	2.48	3.81	2.49
	Relative difference (%)	-13.88	4.20	-5.93	-4.60
	RMSE	0.67	0.51	0.60	0.41
Aerosol profile	z_{aer} [km]	4.9	4.5	4.7	4.7
	Δz [km]			2	
n_i	n_i at 354 nm	0.0395	0.0382	0.0388	0.0314
	n_i at 388 nm	0.0386	0.0366	0.0373	0.0306
	Relative difference between 354 and 388 nm	2.33%	4.37%	4.02%	2.61%
ω_0 at 550 nm	ω_0 (AERONET)	0.89	0.89	0.92	0.91
	ω_0 (DISAMAR)	0.83	0.81	0.87	0.85
	Relative difference (%)	-6.74	-8.99	-5.43	-6.59

780

785

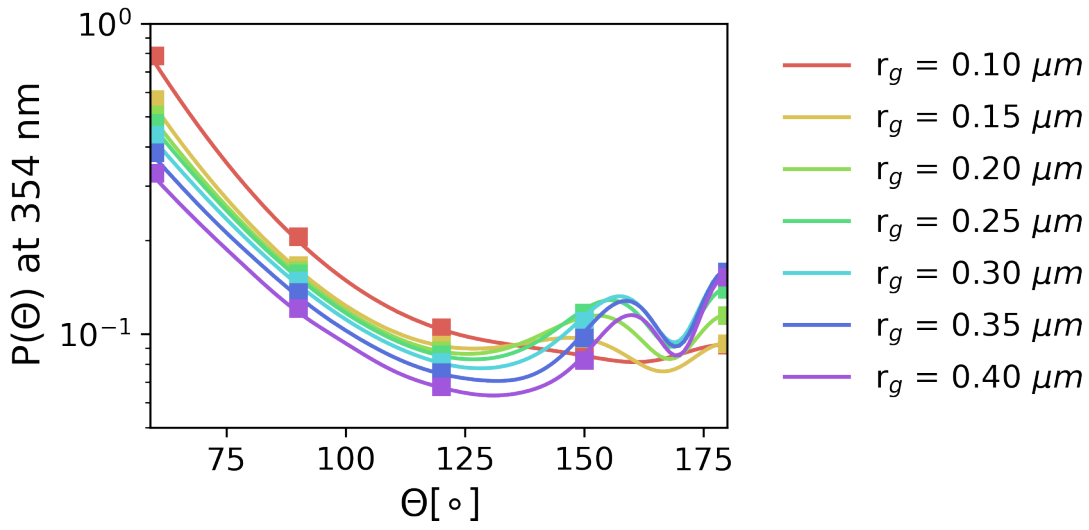
790

795

800

805

Appendix A



810 Figure.A1: Phase function $p(\Theta)$ at 354 nm of the parameterized Mie scattering aerosol in sensitivity studies as a function of r_g (with $n_r = 1.5$ and $n_i = 0.06$). The markers in the plot correspond to values when $\Theta = 60^\circ, 90^\circ, 120^\circ, 150^\circ, 180^\circ$.

815

820

825

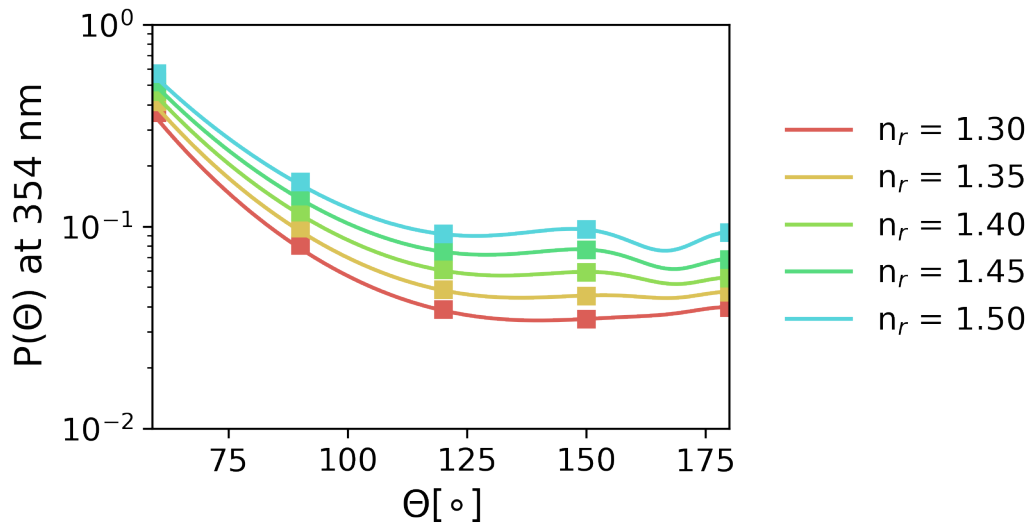
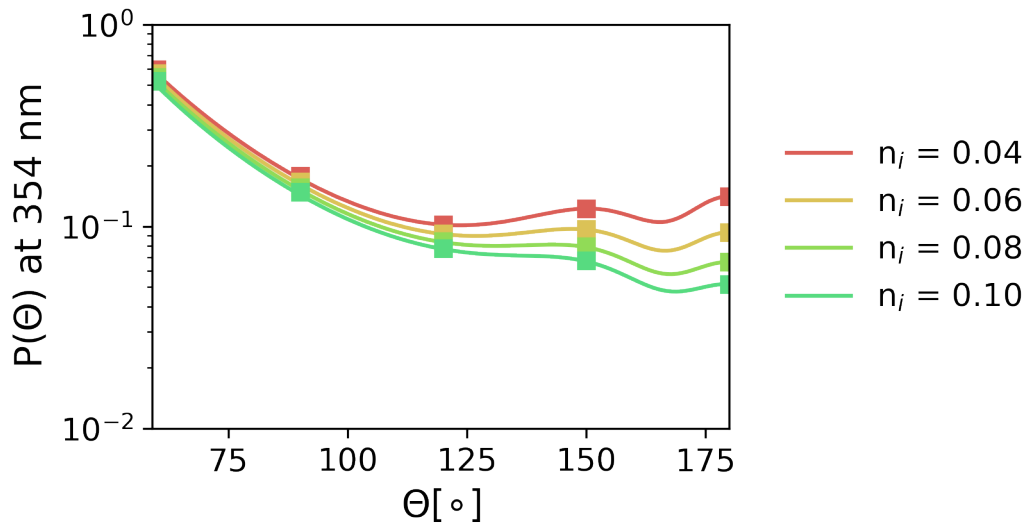


Figure.A2: Phase function $p(\Theta)$ at 354 nm of the parameterized Mie scattering aerosol in sensitivity studies as a function of n_r (with $r_g = 0.15 \mu\text{m}$ and $n_i = 0.06$). The markers in the plot correspond to values when $\Theta=60^\circ, 90^\circ, 120^\circ, 150^\circ, 180^\circ$.

830

835

840



845

Figure.A3: Phase function $p(\Theta)$ at 354 nm of the parameterized Mie scattering aerosol in sensitivity studies as a function of n_i (with $r_g = 0.15 \mu\text{m}$ and $n_r = 1.5$). The markers in the plot correspond to values when $\Theta = 60^\circ, 90^\circ, 120^\circ, 150^\circ, 180^\circ$.